PCCP

Accepted Manuscript

ROYAL SOCIETY OF CHEMISTRY

www.rsc.org/pccp

PCCP

ARTICLE

Rational Design of Hierarchical ZnO Superstructures for Efficient Charge Transfer: Mechanistic and Photovoltaic Studies of Hollow, Mesoporous, Cage-Like Nanostructures with Compacted 1D Building Blocks

Received 00th January 20xx,
Accepted 00th January 20xx

DOI: 10.1039/x0xx00000x

www.rsc.org/

Tridip Ranjan Chetia,[a] Mohammad Shaad Ansari[a] and Mohammad Qureshi[*a]

Mesoporous and hollow zinc oxide (ZnO) hierarchical superstructures assembled with compacted 1D building blocks that provide an efficient and faster transport pathways for photo-generated charge carriers have been synthesized using a biomass derived polysaccharide "Alginic Acid". To understand the interactions among organic bio-template and inorganic growth units of ZnO in aqueous medium, effect of the additives such as alginate ion (ALGI) and ammonium hydroxide (NH_4OH), along with the control reaction conditions are investigated using Field Emission Scanning Electron Microscopy (FESEM) and powder X-ray diffraction. Dynamic and steady-state photoluminescence measurements are carried out to understand the charge transfer processes in the compact 1D superstructures. Experimental analyses reveal that the alginate ions, under hydrothermal reaction conditions, act as a structure directing agent and assemble 1D ZnO nanorods (NRs) hierarchically while NH_4OH assists the formation of ZnO growth units. A plausible formation mechanism of ZnO cages is proposed based on the experimental observations. Morphology dependent photovoltaic properties of ZnO heterostructures, i.e., for ZnO cages, ZnO NRs and ZnO PNPs have been studied along with Electrochemical Impedance Spectroscopy (EIS). A ~60 % and ~35 % enhancement in power conversion efficiency (PCE) is observed in ZnO cage based devices as compared to ZnO NR and ZnO PNP based devices, respectively.

Introduction

Recent advances in the rational design and development of inorganic semiconductor nanomaterials having excellent charge transport and optical properties has received considerable attention among the scientific community.[1-6] Synthetic processes of these materials involve utilization of a range of structure directing agents and additives which can alter the classical arrangement of respective growth units. Among these synthetic methodologies, bio-inspired synthetic approaches utilize naturally abundant chemicals as structure directing agents and allow us to achieve a control over morphology of materials to fascinate exotic electrical, optical, magnetic property, structural speciality, intricacy, and relevant features.[7, 8] In particular, bio-templates are relatively economical and environmentally benign. The control over crystallization of inorganic materials achieved in biomimetic synthetic procedures have been a motivation for the development of new simple synthetic routes to materials of technological interest.[9] For instance, a number of naturally profuse bio-species such as peptides,[10] butterfly wings,[11] shell membrane,[12] cellulose fibers,[13] sodium carboxymethyl cellulose,[14] pollen grains,[15] gelatin,[16] hyaluronic acid and chondroitin-6-sulfate,[17] pectin,[18] etc. are employed as templates in the synthetic methods of inorganic functional materials. In presence of these bio-templates, the crystal growth processes might in certain aspects resemble to mimic the bio-mineralization processes.[19] However, the formation mechanisms of aggregate morphologies are still scarce and need to be understood for better design of materials. It is believed that the formation of aggregates might be inspired by the templating effect of the bio-polymers along with electrostatic force driven, non-classical arrangement of the growth units.[9, 20] In order to achieve novel structures of various materials, it is important to understand the interactions between the soft bio-materials and inorganic materials.

Zinc oxide (ZnO) is an important direct band gap semiconductor which has received extensive research interest due to its unique physical and chemical properties.[21-24] Moreover, transport and optical properties of ZnO can be

[a] Materials Science Laboratory, Department of Chemistry, Indian Institute of Technology Guwahati, Assam, 781039, India.
[b] E-mail: mq@iitg.ernet.in, Tel: +91-361-2582320, Fax: +91-361-2582349

Electronic Supplementary Information (ESI) available: [PXRD patterns of all the products obtained under different reaction conditions along with the tables of calculated crystallite sizes, low magnification FESEM images, TEM analysis of ZnO NRs and ZnO nanoparticles obtained from ZnO PNPs, steady state PL spectra for all the un-sensitized as well as the dye sensitized photoanodes and a table representing current scenario of ZnO Based N719 dye sensitized solar cells and their relevant performance parameters along with present results in our manuscript are discussed in the supporting information]. See DOI: 10.1039/x0xx00000x

tuned by tailoring into various architectures such as zero dimensional (0-D), one dimensional (1-D), two dimensional (2-D) nanostructures as well as three dimensional (3-D) superstructures which opens up potential applicability in wide spectrum of areas. This is possible in case of ZnO partly due to its ease of crystallization and anisotropic growth behavior of crystal planes.[25-27] Among all the heterostructures, synthesis of 3-D superstructures assembled with 1-D nanostructures is a great challenge as they are enriched with superior optical and electrical properties for photovoltaic as well as photocatalytic applications.[2,28] Apart from ZnO, synthesis of 3D superstructures of other important transition metal oxides such as TiO_2, MnO_2, Fe_2O_3 etc. are also performed and achieved promising solar energy harvesting ability.[29-32] 3-D superstructures have the potential to provide high surface area for sensitizer molecule adsorption, excellent light scattering ability along with direct and faster transport pathways for photo-generated electrons.[23] Additionally, porous and hollow characteristics of these materials are conducive to diffusion of electrolyte for better functioning of the redox couple in the photovoltaic devices. Very few synthesis protocols are developed to achieve anticipated superstructures of ZnO by various research groups.[33-37]

Herein, mesoporous and hollow 3-D ZnO superstructures assembled with compact 1D nanorods which can provide faster photogenerated charge transfer pathways are synthesized in a faster (1.5 h) and low temperature (120 °C) hydrothermal synthetic protocol. In the synthetic process we have utilized a soft bio-template alginic acid in the form of sodium alginate (ALG) as a structure directing agent and ammonium hydroxide (NH_4OH) as a precipitating base. ALG is an easily available anionic polysaccharide which is extracted from seaweeds and its chemical structure is depicted in Figure 1. We have optimized the reaction conditions by varying time and the additive sequences of ALG and NH_4OH. Based on the systematic experimental observations, a plausible formation and growth mechanism is proposed for the as-synthesized ZnO superstructures. Technological importance of the material is established by evaluating photovoltaic properties and compared performance parameters with the similar devices fabricated using conventional ZnO morphologies, i.e., ZnO nanorods (NRs) and porous ZnO nanoparticles (PNPs). Improved photovoltaic performance is observed for the devices based on ZnO superstructures over the ZnO NRs and ZnO PNPs.

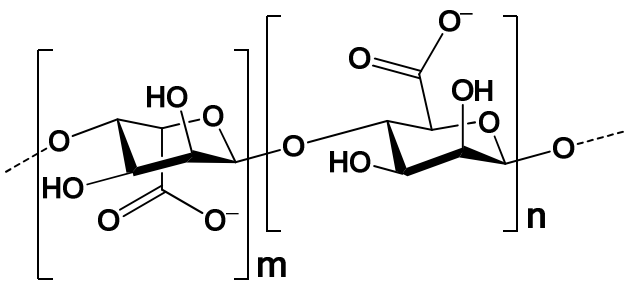

Fig. 1 The chemical structure of sodium alginate in water.

Experimental

Materials

The chemicals and reagents used during the synthesis and preparation were analytically pure and used directly as received without further purification. Zinc nitrate hexahydrate (Merck), sodium alginate (Himedia), ammonium hydroxide (Merck), a triblock copolymer poly(ethylene glycol)-block-poly(propylene glycol)-block-poly(ethylene glycol) or PEG-PPG-PEG (Sigma Aldrich), terpineol (Himedia), chloroplatinic acid (Sigma Aldrich), lithium iodide (Sigma Aldrich), iodine (Merck), 4-tert-butylpyridine (Himedia), acetonitrile (HPLC grade, Merck), valeronitrile (Sigma Aldrich), 1-butyl 3-methyl imidazolium iodide (Sigma Aldrich), methanol (Merck), ethanol (TMEDA) and hydrogen chloride (Merck) are used without further purification. Low temperature thermoplastic films were used as a sealant material (Dyesol). Fluorine doped tin oxide (FTO) coated glass substrates having sheet resistance 12−14 Ω/cm^2 were obtained from Sigma Aldrich USA. The FTOs are used as substrates for fabrication of both the electrodes, i.e., photoanode and cathode. For all the experiments high grade Milli-Q water (18.2 MΩ cm^{-2}) is used.

Synthesis of ZnO cages

The typical synthetic procedure of alginic acid assisted ZnO is as follows. A calculated amount of 0.1 wt % of sodium alginate (0.025 g) is dissolved in 25 mL of Milli-Q water with continuous stirring followed by the addition of zinc nitrate hexahydrate (1 mmol, 0.297 g). Instantly a jelly like precipitate is observed in the solution and there after it is stirred continually for another 15 min. Subsequently, an optimized amount of 25 % NH_4OH (1.5 mL) is slowly added into the solution. It is observed that, immediately after addition of NH_4OH, a white precipitate possibly of $Zn(OH)_2$ appears in the solution. Further addition of NH_4OH upto 0.8 mL to the reaction mixture, the white precipitate disappears completely and become a clear solution. After complete addition of NH_4OH upto 1.5 mL, the pH of the solution is found to be ~10. The clear solution is transferred into a teflon lined stainless steel autoclave, sealed tightly and kept at 120 °C for 1.5 h. After cooling down to room temperature, the precipitate is centrifuged, washed with distilled water and absolute ethanol several times and dried in a hot air oven at 70 °C for 6 h. Control reactions in absence of NH_4OH and sodium alginate respectively are carried out. We have also investigated the reaction in detail by varying addition sequences of NH_4OH and ALG keeping other reaction conditions same in the order to gain insights into the effects of both the additives. In addition, reactions are carried out at different interval of time, i.e., for 40 min, 60 min, 90 min and 120 min so as to follow and understand the growth process of the superstructures.

Fabrication of photoanodes and devices

All ZnO based photoanodes were fabricated by making a homogenous paste of Zinc oxide and pasted it over the conductive glass substrates i.e. FTO. For the preparation of ZnO paste, ZnO powder (0.1 g) was ground with a mixture of terpineol and triblock copolymer (PEG-PPG-PEG) in an agate

mortar until a homogenous paste was formed. This homogenous paste was coated on pre-cleaned conductive glass substrate i.e. FTO via doctor blade technique and the films were dried in air, followed by calcination at 520 °C for 60 min to remove the polymer. The thickness of the ZnO layer was measured by a surface profilometer (Veeco Dektak-150) and it was found to be in the range of 12–15 µm. These substrates were then immersed into N719 dye solution in ethanol (0.3 mM) for 2.5 h at 50 °C. The sensitized photoanodes were taken out from dye solution, washed with absolute ethanol and dried in hot air blow. The dye sensitized solar cell (DSSC) devices were fabricated by sandwiching the photoanodes and counter electrodes. To fabricate the counter electrode, a solution of 5 mM chloroplatinic acid in isopropanol was spin coated on a cleaned, ozonized FTO substrate. The spin coated FTO substrate was then calcined at 450 °C for 30 min (heating ramp of 5 °C/min) in a muffle furnace. The furnace was cooled down to room temperature naturally and taken out the as prepared platinum coated counter electrode. The electrolyte solution was introduced to the devices after sealing (using low-temperature thermoplastic sealant, thickness ~50 µm) through a hole in the counter electrode which was made by drilling using a glass driller. The I^-/I_3^- electrolyte solution was prepared by dissolving 0.5 M LiI, 0.05 M I_2, 0.1 M guanidium thiocyanate, and 0.5 M 4-tert-butylpyridine in a solvent mixture of acetonitrile: valeronitrile (9:1, v/v). The active area for all fabricated devices were fixed and it was found to be 0.25 cm^2. Before the photovoltaic measurements i.e. (I–V), IPCE and EIS measurements, the fabricated devices were kept under dark condition for 24 h.

Measurements and Material Characterization

The powder X-ray diffraction (PXRD) measurements were carried out by using Bruker D2 Phaser X-ray diffractometer having Cu–Kα (λ= 1.54 Å) X- ray source. The operating voltage and current were 30 kV and 30 kA respectively. The scan rate was fixed at 0.1 °/s for recording the XRD patterns within 2θ range of 10–80°. The UV–vis diffuse reflectance spectra (DRS) were recorded via a JASCO Model V-650 spectrophotometer by using 150 mm integrating sphere and $BaSO_4$ used as an internal standard. Steady state photoluminescence (PL) studies were carried out using a Horiba–Jobin Yvon Fluoromax 4 spectrophotometer. Beckman-Coulter SA 3100 N_2 adsorption apparatus was used for Brunauer–Emmett–Teller (BET) surface area analysis. Prior to surface area analysis, the samples were degassed at 150 °C for 3 h. The morphology of the as synthesized materials were investigated by performing field emission scanning electron microscopy (FESEM). A FESEM instrument, manufactured by Zeiss (Model: Sigma) was employed to take the images. The transmission electron microscopy (TEM) measurements were performed on a JEOL JEM 2100 microscope with an operating voltage of 200 kV. Veeco Dektak-150 surface profilometer was used to measure the thickness of the ZnO layer deposited onto FTO substrates. Current density–voltage (*J–V*) measurements for the fabricated devices in dark and for light illumination were carried out under an AM 1.5G artificial solar light of 100 mW/cm^2 and recorded using a Keithley 2400 source-meter. Calibration of the arc lamp (intensity 450 W) of Newport ORIEL Sol3A solar simulator was done by a standard Si photovoltaic cell. Newport ORIEL IQE-200 instrument fitted with 250 W quartz tungsten halogen lamp was employed to record incident photon to current conversion efficiencies (IPCE) of the fabricated devices. The electrochemical impedance spectroscopy (EIS) measurements were performed by using CH instruments model CHI680E, Inc., Austin, TX.

Results and Discussions

Powder X-ray Diffraction Analysis

Figure 2(A) depicts powder X-ray diffraction (PXRD) patterns and intensity variation of the peaks for crystal planes $(10\bar{1}0)$, (0002) and $(10\bar{1}1)$ of as synthesized ZnO heterostructures. Trace (a) represents PXRD pattern of ZnO synthesized in presence of both ALG and NH_4OH (reaction 1). Traces (b) and (c) are for the ZnO synthesized in the control reactions; in presence of only NH_4OH (reaction 2) and in presence of only ALG (reaction 3). It is observed that an amorphous product is obtained, presumably an adduct of Zn^{2+} with alginate ions in the reaction 3 [trace (d)] which is converted into pure ZnO after calcination at 520 °C for 1 hour as evident from the PXRD patterns, traces (c) and (d). Crystal phase for all the three type of ZnO are defined to be hexagonal wurtzite phase with $(10\bar{1}0)$, (0002), $(10\bar{1}1)$, $(10\bar{1}2)$, $(11\bar{2}0)$, and $(10\bar{1}3)$ planes with a $P6_3mc$ space group symmetry and Zn atoms in tetrahedral sites according to the JCPDS Card No. 36-1451 (Figure S1, see ESI). No peaks due to impurity are detected in the PXRD patterns which infers that as-synthesized products are pure ZnO with good crystalline characteristics.

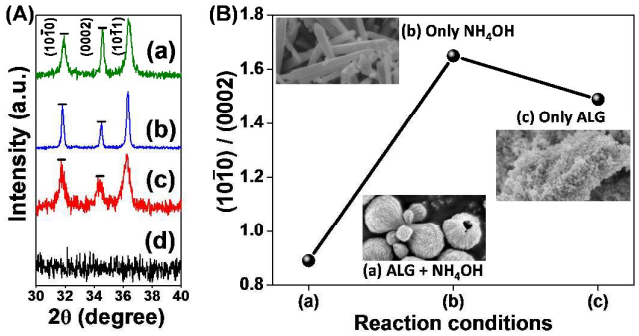

Fig. 2 (A) Powder X-ray diffraction patterns of the products synthesized under different reaction conditions showing intensity variation of the peaks for $(10\bar{1}0)$, (0002) and $(10\bar{1}1)$ crystal planes of ZnO, in presence of (a) both ALG and NH_4OH (reaction 1) (b) only NH_4OH (reaction 2) (c) only ALG after calcination and (d) before calcination (reaction 3). **(B)** Plot of $(10\bar{1}0)/(0002)$ intensity ratio obtained from the spectrum (a), (b) and (c) of figure 1 (A) vs all the ZnO nanostructures synthesized under three reaction conditions namely (1), (2) and (3). Insets to figure 1(B) show FESEM images of (a) ZnO Cages, (b) ZnO Nanorods (NRs) and (c) ZnO Porous Nanoparticles (PNPs).

It is noteworthy that the intensity ratio of $(10\bar{1}0)$ to (0002) crystal planes varied significantly for all the three type of ZnO which is indicative of differential tropism of the products in the three reaction conditions namely reaction 1, 2 and 3.[38] A

smaller value of $(10\bar{1}0)/(0002)$ ratio indicates the formation of ZnO rods showing a preferential growth along the c-axis which also reflects the larger number of planes along the (0001) direction of the rod, whereas a larger value of $(10\bar{1}0)/(0002)$ ratio specifies inhibited growth along the c-axis.[39, 40] Figure 2(B) represents a plot of $(10\bar{1}0)/(0002)$ intensity ratio obtained from the PXRD patterns (a), (b) and (c) of figure 1(A) vs all the ZnO nanostructures synthesized under three reaction conditions. From figure 2(B) it is pragmatic that the increasing order of $(10\bar{1}0)/(0002)$ intensity ratio for the ZnO obtained from the reactions (1), (2) and (3) is : (a) ALG + NH_4OH or reaction 1 <(c) Only ALG or reaction 3 <(b) Only NH_4OH or reaction 2. Lowest value of $(10\bar{1}0)/(0002)$ intensity ratio for ZnO obtained in the reaction 1 infers crystal growth anisotropy along longitudinal c-axis while higher values obtained from the products of reactions 2 and 3 suggests inhibited growth along c-axis. Topographies and dimensions of the products are further confirmed from FESEM analysis as we have displayed in the insets of figure 2(B). In case of the reaction 1, ZnO superstructures assembled with tiny 1D ZnO nanorods are attained while ZnO nanorods (NRs) and ZnO porous nanoparticles (PNPs) are formed in the reaction conditions (2) and (3) respectively. The FESEM analysis of the products obtained from reaction 1 and 3 are in good agreement with the inferences carried out about crystal growth habit of ZnO from PXRD patterns on the basis of previous reported works, while it is not in the case of ZnO obtained from reaction 2. It is expected that the structure of ZnO in this case should be nanoparticles or nano-disks with less number of crystal planes along c-axis, i.e. (0001) direction, whereas it is observed to be the formation of ZnO nanorods. This observation might be due to the random arrangement of ZnO NRs in the horizontal plane of the substrate which causes less exposure of the crystal planes along (0001). It should be mentioned that if maximum number of ZnO NRs are aligned vertically on the substrate (i.e., normal to the substrate), strong appearance of (0002) diffraction peak at ($2\theta \approx 34.61°$) is noted (Figure S2, see ESI). However, in case of ZnO superstructures numerous tiny ZnO NRs (diameter in the range ~8-10 nm) are hierarchically arranged which increases the percentage of vertically aligned ZnO NRs and consequently upsurges the intensity of the peak (0002) from the crystal planes along (0001) direction.

Material morphology

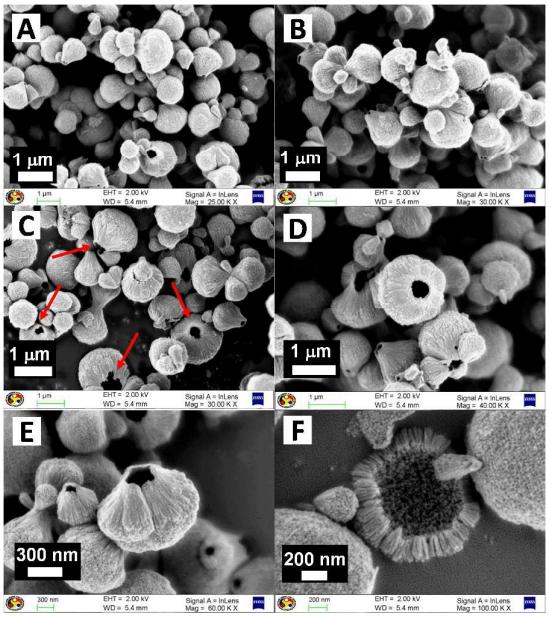

Fig. 3 FESEM images (A, B, C, D and E) of as synthesized cage like ZnO superstructures at different magnifications. Image (F) shows a broken ZnO superstructure.

Figure 3 (A, B, C, D and E) shows the FESEM features of as-synthesized cage like ZnO superstructures at different magnifications. From the FESEM images (A), (B) and (C) we have seen that as synthesized product comprises of both multi-cage and single cage 3D ZnO superstructures. The average longitudinal dimension of the ZnO multi-cage structures are in the range of 2-3 µm and ~1 µm for a single cage ZnO. Each multi-cage superstructure is composed of two main bigger cages adjoined opposite to each other, which are observed to be of similar size; while the branched cages growing from the adjoining point are smaller and have random size distribution. Consequently, there will be three types of ZnO cages in the sample namely: (a) multi-cage ZnO, (b) bigger size single cage ZnO [indicated with red arrows in image (C)] and (c) smaller size single cage ZnO. It is obvious that the latter two type of cages [i.e., (b) and (c)] are originating due to fracture of multi-cage ZnO at the adjoining points. However, the presence of smaller cage ZnO is expected to be beneficial for the fabrication of photoanode with higher light harvesting ability. It can be ascribed to the high probability of smaller cage ZnO to occupy the voids produced in between the bigger size single cage ZnO and multi-cage ZnO. This in turn will improve the inter-particle electrical connectivity to act as the photoinduced electron channels that leads to an increase in the current density (J_{sc}) value as well as light scattering. Figure 3(D) and (E) are FESEM images representing top and side view of ZnO cages at higher resolution. The width of the as obtained ZnO cages is around 1-1.5 µm and are open with a macropore of diameter ~300 nm. The pore is representing the adjoining point of the cages in the multi-cage ZnO superstructures resulting from the detachment of the cages and is confirming the hollow characteristic of the material. It is observed that the ZnO cages are composed of numerous tiny ZnO NRs. Figure

3(F) shows a cracked ZnO cage at higher magnifications which confirms hierarchical arrangement of the nanorods to form ZnO superstructures. The attachment of the nanorods with different lengths is leading to formation of pores in-between them and thereby these superstructures may behave as mesoporous material. Furthermore, we have performed TEM and surface area analysis (BET measurements) to verify the morphological conclusions carried out from FESEM analysis.

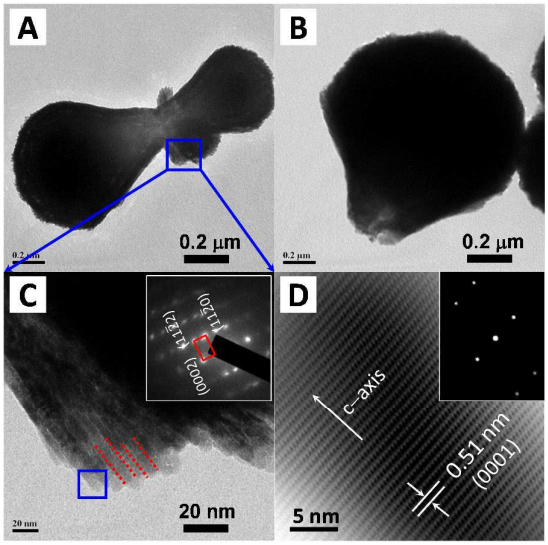

Fig. 4 TEM images (A) and (B) are showing a multi-cage and a single cage ZnO superstructure respectively. High resolution transmission electron microscopy (HRTEM) image of the ZnO superstructure (trace C) and inset to it shows related SAED pattern. Trace (D) represents Inverse fast Fourier transform (IFFT) of atomic planes for the specified part of trace (C) with corresponding FFT in the inset.

The TEM images figure 4(A) and (B) are representing a multi-cage and a single cage ZnO superstructures respectively. The high resolution TEM image [trace (C)] reveal that the ZnO cages are composed of a number of tiny ZnO NRs with diameter ~8-10 nm which is in accordance with the FESEM analysis. The density of ZnO NRs at the adjoining point of the ZnO cages is minimum which is divulged through the higher transparency towards electron beam at these points [Images 4(A) and (B)]. Accordingly, mechanical strength of the multi-cage ZnO superstructures at the adjoining point will be very less which is the most probable cause for detachment of the superstructures at this specific point. The selected area electron diffraction (SAED) pattern of ZnO cages is indexed as $(1\bar{1}00)$ zone axis and is shown in the inset to figure 4(C). The red dotted lines in figure 4(C) indicates two adjacent ZnO NRs. The SAED pattern is unfolding the wurtzite single crystalline structure of each ZnO NRs and crystal growth anisotropy along (0002) crystal planes which is consistent with the PXRD results [Figure 2(A) and (B)]. The Inverse Fast Fourier Transform (IFFT) of atomic planes is carried out for the indicated part of trace 4(C) and is as depicted in the figure 4(D). The interplanar distance of the crystal planes is found to be ~0.51 nm which is for (0001) crystal planes accrediting the preferable crystal growth along the c-axis or the (0001) direction. Inset to figure 4(D) is the related Fast Fourier Transform (FFT) pattern and verifies the single crystalline nature of the ZnO NRs.

In order to understand the growth mechanism and evolution of cage like morphology of ZnO superstructures we have investigated the reaction in detail using controlled conditions by varying the addition amount of NH_4OH, ALG and reaction times. The change in morphological characteristics and crystallinity of the products are monitored by performing FESEM and PXRD analysis respectively.

Effect of ammonium hydroxide (NH_4OH). In order to realize the role of NH_4OH in the growth process of the cage like ZnO superstructures, we have carried out the reactions by sequentially varying amount of NH_4OH per 25 mL of the reaction mixture. It should be noted that the amount of ALG added and the time of the reaction kept constant at 0.1 wt % and 1.5 h.

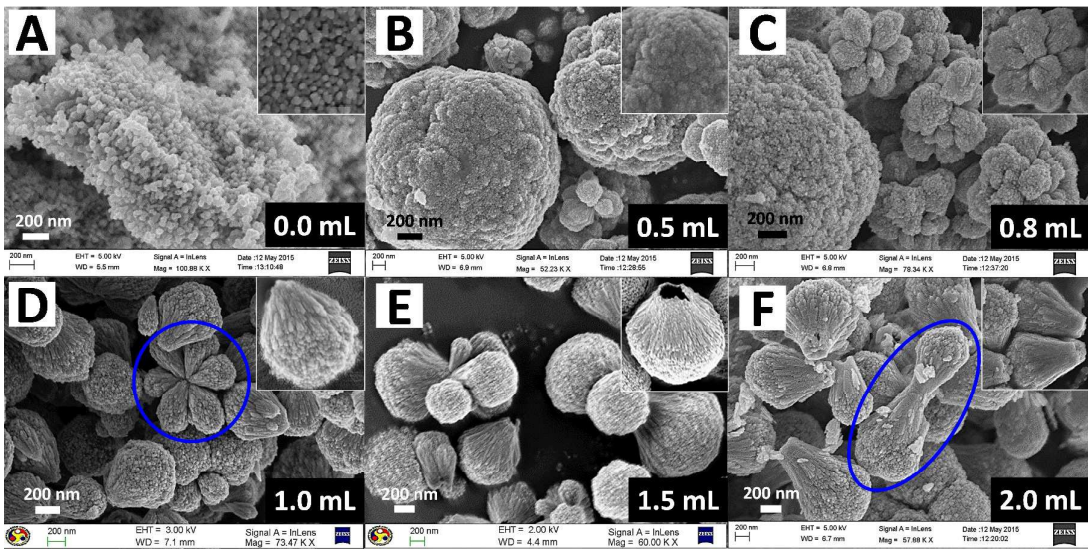

Fig. 5 FESEM features of the as prepared products with different amount of NH_4OH: (A) 0.0 mL, (B) 0.5 mL, (C) 0.8 mL i.e., at the precipitate disappearing point, (D) 1 mL, (E) 1.5 mL and (F) 2 mL. Insets show corresponding higher magnification FESEM images for better clarity.

Control reactions are performed by varying the amount of NH_4OH from 0.0 mL to 2.0 mL with an increment of 0.5 mL and topographies are presented in figure 5. Additionally, a reaction at 0.8 mL of NH_4OH is also carried out, wherein we have observed a sudden disappearance of gelatinous precipitate. Observation of a gelatinous precipitate could be due to an amorphous complex formation, ALGI–Zn^{2+} [Figure S3, trace (a); and Figure S4, trace (A), see ESI]. After calcination at 520 °C for 1 h in a muffle furnace, it translates into aggregates of ZnO nanoparticles with pores (abbreviated as ZnO PNPs) in the range of 10-20 nm respectively as we have observed from trace (A), figure 5. BET surface area analysis for the sample is conducted and discussed in later. The size of the nanoparticles are in the range of 10–15 nm and single crystalline as confirmed from TEM analysis (Figure S5, see ESI). On addition of 0.5 mL NH4OH to the reaction mixture, two types of spherical ZnO aggregates, one with a size distribution of ~(0.5–1) µm and another with ~(1–3) µm are observed, trace (B). Further addition of NH_4OH (upto 0.8 mL), i.e., the precipitate disappearing point, results in the formation of star shaped co-joined lobes of ZnO (size ~0.5 µm–1 µm) along with the spherical aggregates (size range ~1 µm–3 µm). Increase in the amount of NH_4OH to 1.0 mL, leads to the formation of cage like ZnO with smaller diameter (~500 nm) of uniform size distribution [see Trace (D) and Figure S4, image (E) in ESI]. Although, these cages are originating from the flower like superstructures as indicated in the image (D), the adjoining points of the single cages are not open. Image (E) manifests the anticipated ZnO cages with open hollow structures obtained on addition of 1.5 mL of NH_4OH. The crystallinity of this product is also observed to be superior relative to all others [Figure S3, trace (f), see ESI], including the structures acquired in case of 2.0 mL NH_4OH as displayed in the image (F). Hence, the optimum amount of NH_4OH to be added in the reaction is found to be 1.5 mL per 25 mL of the reaction mixture and is kept constant in further reactions. The size distribution of the ZnO cages perceived in the reaction of 2.0 mL of NH_4OH, is noted to be very similar to that obtained in the reaction with 1 mL [Figure S4, image (G); see ESI]. However, dumbbell shaped structures of ZnO are appeared as indicated in the image (F), instead of flower like superstructures as in case of 1 mL NH_4OH. From all the above discussions it is clear that the addition of NH_4OH in the reaction have a profound effect on the material morphology as well as in the crystallinity of the superstructures. It is also clear that only the addition of NH_4OH facilitates the formation of ZnO in hydrothermal conditions, confirms that the growth units are $Zn(OH)_4^{2-}$ and $Zn(NH_3)_4^{2+}$. It is well known that, NH_4OH could provide both NH_3 and OH^- ions to the aqueous solution and both are good coordinating ligands of Zn^{2+}.[41] In scheme 1, we have schematically represented the controlled reaction condition pathways for the formation of ZnO superstructures in presence alginate ion by varying the concentration of NH_4OH.

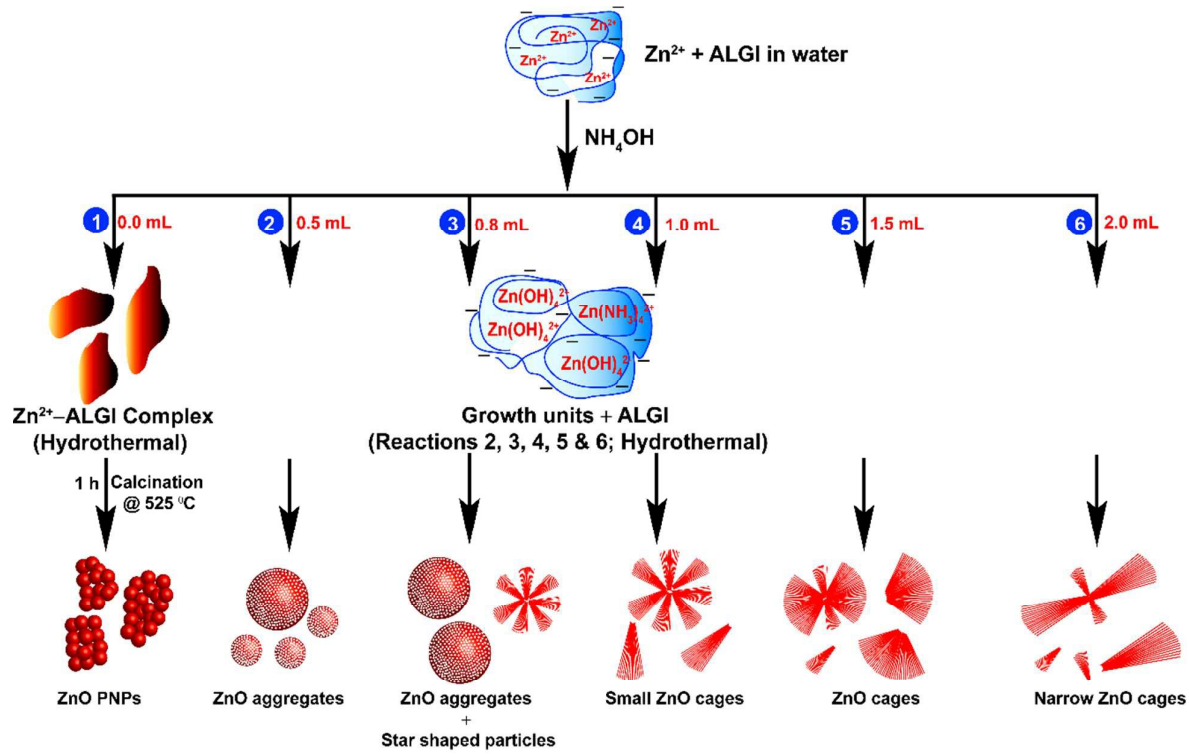

Scheme 1 Effect of ammonium hydroxide (NH_4OH) on morphology variation of ZnO.

PCCP

ARTICLE

ZnO cages are observed to be formed in the reaction which is carried out in presence of both ALG and NH_4OH. Therefore, it is important to understand the effects of the "bio-template" in the growth process of the superstructures.

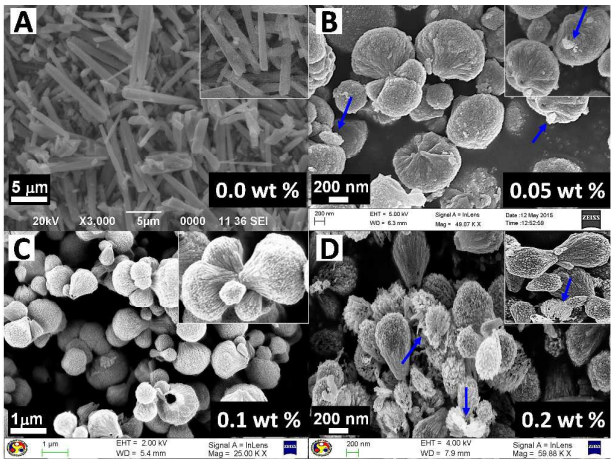

Fig. 6 FESEM images of the as synthesized products with different amount of ALG: (A) 0.0 wt %, (B) 0.05 wt %, (C) 0.1 wt % and (D) 0.2 wt %. Insets show corresponding higher magnification FESEM images for better clarity.

Effect of sodium alginate (ALG) addition. To further prove the effect of bio-template, reactions are carried out by varying the concentration of ALG from 0.0 wt % to 0.2 wt% and FESEM images are shown in the figure 6. The amount of NH_4OH and temperature of the reactions are kept constant at 1.5 mL and 120 °C respectively. Formation of ZnO nanorods with diameter in the range 300 nm–400 nm are observed with only NH_4OH in the absence of ALG (0.0 wt %) as portrayed in the image 6(A) and in its inset. These nanorods are single crystalline having hexagonal wurtzite crystal structure with a preferential crystal growth along (0001) direction as resolved from the SAED and IFFT patterns respectively [Figure S6 (A) and (B), see SI]. Reaction with an increase in the concentration of ALG to 0.05 wt % of ALG, bigger size ZnO cages (longitudinal diameter ~2 µm) along with some irregular multi-cages and tiny aggregates are noticed as indicated with blue arrows in the figure 6(B) and inset to it [Figure S7, trace (B); see SI]. The tiny ZnO aggregates may be due to presence of excess NH_4OH compared to ALG which lead to higher number of growth units [i.e., $Zn(NH_3)_4^{2+}$ and $Zn(OH)_4^{2-}$] in the reaction mixture relative to the alginate ions (ALGI) and random crystal growth of them (note that the concentration of NH_4OH is fixed at 1.5 ml). In contrast, uniform multi-cages as well as single cages of ZnO are appeared in case of the reaction with 0.1 wt % ALG; trace (C) and inset to it [Figure S7(C), see SI]. Further increase in the amount of ALG upto 0.2 wt %, partially formed ZnO cages are observed [indicated with blue arrows in image (D) and inset to it], which is possibly due to inhibited crystal growth of ZnO in presence of excess ALGI. It is noteworthy that the carboxylate groups in the ALGI can preferentially bind to the Zn-populated (0001) crystal planes of the ZnO crystallites and adhere on the surface of them to impede the favorable longitudinal c-axis growth as well as the lateral growth of ZnO crystal in hydrothermal condition.[38] This claim is also in accordance with the formation of larger size ZnO NRs (length ~8–10 µm, diameter ~300–400 nm) in the controlled reaction carried out in absence ALG compared to the nanorods in the superstructures (length ~0.5–0.8 µm, diameter ~10–15 nm). For better clarity, we have shown corresponding low magnification FESEM images in the supporting information (figure S7, see ESI). The above discussions are establishing the optimum amount of ALG to be employed in the reaction is 0.1 wt % which results in uniform and high crystalline ZnO superstructures compared to the products obtained in both the reactions with 0.05 wt% and 0.2 wt %. However, the crystallinity of the ZnO NRs obtained in the controlled experiment is highest (PXRD analysis and figure S8 in ESI) among all the synthesized products and is unveiling the role of ALG as a crystal growth inhibitor and structure directing agent.

Effect of reaction time. For all the aforementioned reactions we have maintained the reaction time at 90 min. In order to optimize the time of the reaction and explore the growth behaviour of ZnO superstructures, morphological characterization of the material at different interval of time (i. e., from 40 min to 120 min) is carried out and are depicted in the figure 7. Variation of crystallinity is also probed for all the products from PXRD patterns and is discussed in the supporting information (Figure S9, see ESI).

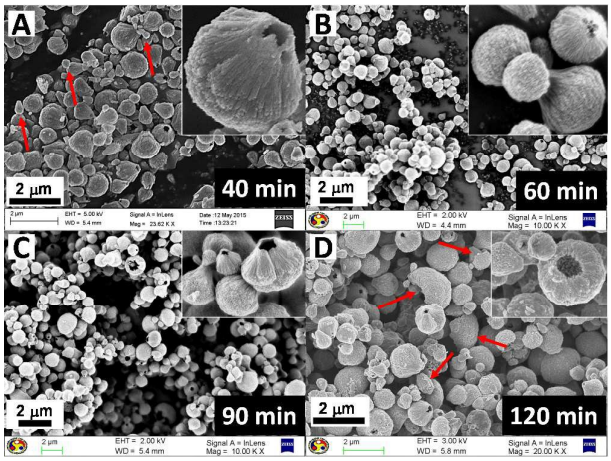

Fig. 7 FESEM topographies of the as obtained products by varying time i.e., after : (A) 40 minute, (B) 60 minute, (C) 90 minute and (D) 120 minute. Insets show corresponding higher magnification FESEM images for better clarity.

Morphology of the product at 40 minute (min) of reaction time is represented in the image (A) and inset to it, figure 7. Cage like ZnO with hollow characteristics are observed in this case. However, partially developed narrower and smaller size cages are also observed [indicated with red arrows in image (A); Figure S10(A), see ESI]. This is an indicative of incompletion of reaction and is confirmed from the low crystallinity of the product compared to the other two cases, i.e., reactions with 60 min and 90 min (Figure S9, see ESI). Although, the morphology of ZnO cages perceived in the reaction time at 60 min and 90 min are very similar as we have seen from trace (B) and (C) respectively, the crystallinity of the later is superior to the former. This implies that an adequate time is achieved by the product, for aging in the reaction with time at 90 min which allows most possible regular arrangement of the ZnO crystal planes. Further, with an increase in the reaction time to 120 min, dissolution of the superstructures is noted, as evident from the high magnification FESEM image portrayed in the inset of the image (D), figure 7. The dissolution of ZnO in wet chemical synthetic process is an inherent characteristic of the material, which leads to decrease in crystallinity.[41] The dissolution effect becomes more dominant in case of prolonged reaction time. Growth process reaches a certain equilibrium with the growth units; $Zn(OH)_4^{2-}$ and $Zn(NH_3)_4^{2+}$ after the formation of ZnO cages. As the reaction progresses, concentration of $Zn(OH)_4^{2-}$ and $Zn(NH_3)_4^{2+}$ is decreased. In order to maintain the equilibrium, dissolution process of ZnO cages in the reaction occurs and results in degraded ZnO cages with poor crystallinity. The PXRD analysis of the material is also in good agreement with the FESEM observations (Figure S9, see ESI). The increase in population of broken ZnO cages in this case, as indicated with red arrows in image (D), infers excess reaction time [Figure S10(B), see ESI]. Therefore, the optimum time for the completion of the reaction is established to be at 90 min.

Evolution process and mechanism of ZnO superstructure formation

Based on all the above discussions, the plausible formation mechanism of ZnO cages at optimized reaction conditions can be explained from scheme 2.

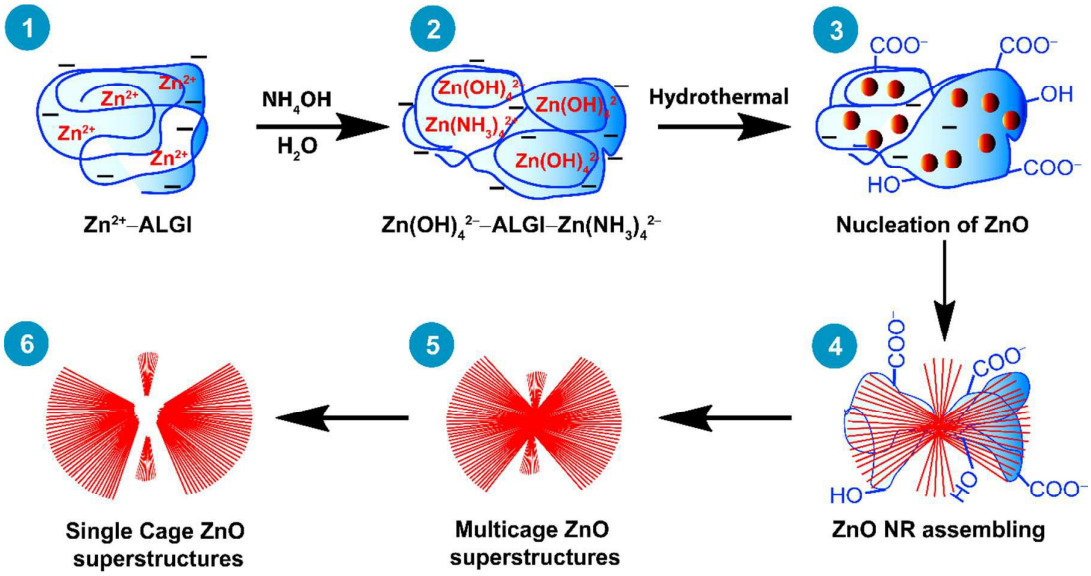

Scheme 2 Schematic representation of step by step evolution process of the ZnO cage formation in the reaction.

Alginic acid is a linear copolymer of 1→4 covalently linked β-D-mannuronic acid and its C-5 epimer α-L-guluronic acid residues in different sequences to construct the backbone chain. Sodium salt of alginic acid, i.e., sodium alginate (ALG) is a naturally abundant polysaccharide or a "biopolymer" extracted from the cell walls of brown seaweed. It is soluble in water and ionizes to its anionic form, i.e., the alginate ion (see figure 1). 0.1 wt % solution of ALG in water is found to be negatively

charged with zeta potential (ζ) ≈ –60 mV. These negatively charged alginate ions with carboxylate groups interact with the positively charged Zn^{2+} ions in the solution due to electrostatic forces and form a complex (1): [Zn^{2+}–ALGI].[38] This complex appears in the reaction mixture as a gelatinous precipitate which is formed immediately after the addition of $Zn(NO_3)_2.6H_2O$ to the solution of ALG. We have probed the formation of complex [Zn^{2+}–ALGI] by performing Fourier transform infrared spectroscopy (FTIR) analysis for the gelatinous precipitate extracted from the reaction mixture and discussed in the supporting information (figure S11, see ESI). On addition of NH_4OH, initially water insoluble white precipitate possibly of $Zn(OH)_2$ is observed. Further addition of NH_4OH upto the optimized amount, i.e., 1.5 mL per 25 mL, the aqueous solution becomes transparent and pH is found to be ~10 which infers the formation of water soluble $Zn(OH)_4^{2-}$ and $Zn(NH_3)_4^{2+}$ ions. It is well known that, $Zn(OH)_4^{2-}$ and $Zn(NH_3)_4^{2+}$ act as the growth units of ZnO crystal in the wet chemical reactions carried out in basic conditions.[42] Subsequently, due to Coulombic interactions the $Zn(OH)_4^{2-}$ and $Zn(NH_3)_4^{2+}$; growth units are believed to be attached with the negatively charged alginate ions to form an adduct complex (2): [$Zn(OH)_4^{2-}$–ALGI–$Zn(NH_3)_4^{2+}$]. In hydrothermal reaction conditions, the growth units initiate the nucleation process and form numerous nuclei of ZnO. These ZnO nuclei tend to grow along (±) *c*-axes, i.e., along Zn^{2+} populated +(0001) and O^{2-} populated –(0001) high energy polar crystal facets promoted by $Zn(OH)_4^{2-}$ and the $Zn(NH_3)_4^{2+}$ growth units respectively which are leading to the formation of ZnO NRs.[43] Since, the ZnO crystal growth along (–) *c*-axis is the slowest growth direction, predominant growth units are $Zn(OH)_4^{2-}$ ions.[44] Simultaneously, the negatively charged alginate ions with (–COO^-) groups anchors to the positive Zn^{2+} populated +(0001) crystal facets of ZnO and adheres on the surface of ZnO NRs. Thus, the growth of ZnO NRs in presence of ALG is inhibited due to the minimized contact between the growth units and (0001) crystal surfaces. Additionally, the free (–OH) and (–COO^-) groups in the ALGI backbone chain, triggers the assembling process of ZnO NRs and arrange hierarchically to form ZnO superstructures as shown in the step 4. At this step, the existence of optimum amount of NH_4OH and an equilibrium between gas–liquid in the autoclave are the crucial factors to acquire the anticipated size and shape of the product. As the reaction proceeds, some of the multi-cage super-structures fracture at the adjoining points and result in single cage superstructures.

UV-Visible absorption and photoluminescence analyses

Figure 8(A) represents UV-Visible absorption spectra for all the synthesized ZnO heterostructures, i.e., ZnO cages (red line), ZnO NRs (blue line) and ZnO PNPs (black line). We have observed a moderate red shift of absorption onset in case of ZnO NRs (~25 nm) and ZnO PNPs (~30 nm) as compared to the ZnO cages. This may be due to smaller size distribution of ZnO NRs (~8-10nm) in the superstructures relative to the particle size distribution in the other two samples (~1 µm and ~2 µm respectively). Optical band gap values for all the samples are estimated from corresponding Tauc's plots as depicted in the inset to figure 8 (A), considering ZnO as a direct bandgap material. In Tauc's plot, $(\alpha h\nu)^2$ is plotted against the photon energy (hν), where α is the absorption coefficient. The band gap values of ZnO hetero-structures are estimated as 3.2 eV for ZnO cages, 3.06 eV for ZnO NRs and 2.95 eV for ZnO PNPs. The observed lowering of band gap values for ZnO PNPs and ZnO NRs in contrast to ZnO cages is in accordance with the red shift of absorption profiles.

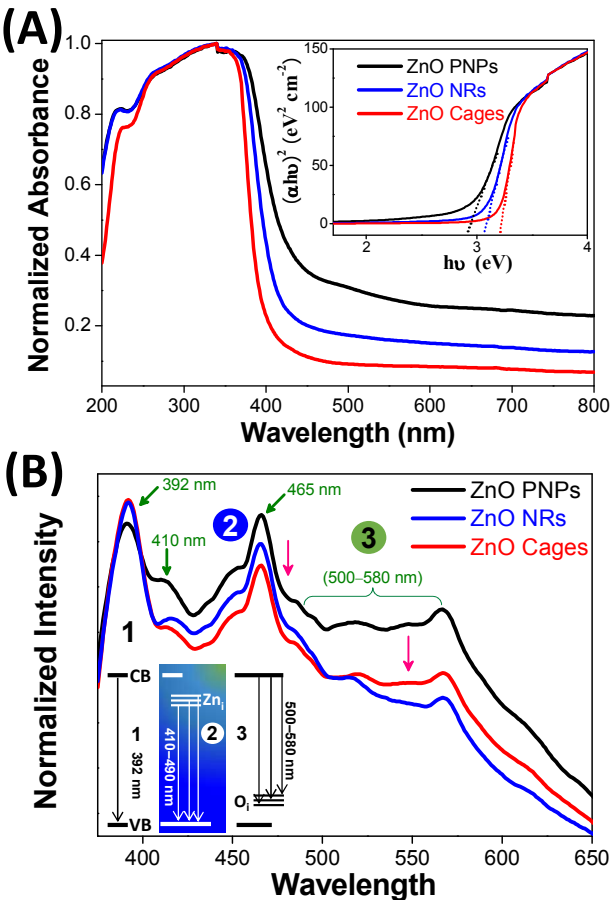

Fig. 8 (A) UV-Visible absorption profiles for all the ZnO heterostructures (ZnO PNPs, ZnO NRs and ZnO Cages). Inset to it shows corresponding Tauc's plots. **(B)** Room temperature steady state photoluminescence (PL) spectra for all the ZnO heterostructures. Inset to it shows the corresponding electronic transitions of the peaks indicated in the spectra with green arrows.

The emission characteristics and defect states of all three different morphologies of ZnO are analysed by performing room temperature steady state photoluminescence (PL) spectroscopy at an excitation wavelength of 355 nm and illustrated in Figure 8(B). For all the samples, sharp emission in the UV range (~395 nm) followed by a shoulder around 410 nm and sharp peak at ~465 nm are noticed. A green broad emission band with satellite peaks at around ~500-580 nm are also observed. The sharp emission in the UV range signifies near-band-edge emission which is attributed to radiative exciton annihilation[45] as depicted in the inset (1). The shoulder peak around 410 nm and the sharp peak ~465 nm are

originating from co-ordinatively unsaturated Zn^{2+} interstitial sites (Zn_i, shallow donor) in the ZnO nanostructures [see corresponding transitions in the inset (2)]. The emission peaks observed in the broad visible region (i.e., 500-580 nm) are accredited to the transitions from the conduction band to the deep trap levels of ZnO (created by oxygen vacancies in the ZnO crystal structure, O_i), as shown in the inset (3).[45, 46] From figure 8(B), it is clear that the intensity of near band-edge emission are comparable for ZnO NRs and ZnO cages while for ZnO PNPs the intensity is appreciably decreased. However, the intensity of the emission peaks due to zinc and oxygen defect sites are higher for ZnO PNPs as compared to ZnO NRs and ZnO cages. This is a clear reflection of higher population of defect sites in ZnO PNPs relative to the ZnO NRs and ZnO cages. This observation may be due to maximum population probability of grain boundary induced defect sites in ZnO PNPs, as they are composed of numerous inter-connected ZnO NP.

Further, to gain insights into the variation of defect sites in the photoanodic films after the calcination, we have performed steady state and dynamic photoluminescence measurements (Figure S12, see ESI). Form figure S12, we have observed that, calcination of photoanodes at 520 °C for 1h in a muffle furnace, intensity of broad emission band in the visible region (~500-580 nm) which is attributed to the oxygen vacancies (or O_i) in the ZnO crystal structure is reduced. Among all the three samples, maximum reduction of oxygen vacancy distribution is observed in case of ZnO cages while it is minimum for ZnO PNPs. However, intensities of shoulder peak around 410 nm and the sharp peaks ~465 nm are slightly higher for ZnO cages which is an indicative of higher concentration of Zn_i defects sites in the photoanode than its counterparts, i.e., ZnO NR and ZnO PNP.

The exciton lifetime in ZnO cages before and after the calcination is monitored by time resolved PL (TRPL) analysis to understand the charge transport kinetics in the photoanode as shown in figure 9. Note that, the calcination temperatures were kept intentionally at 520 °C in order to have a match with the fabrication of photoanodes, where in a similar temperature regimes were used to remove the binder and the other additives.

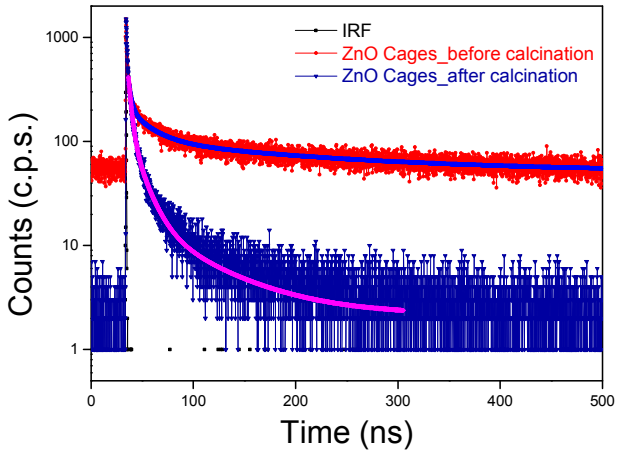

Fig. 9 Time resolved photoluminescence spectra for ZnO Cages recorded at an excitation wavelength 355 nm before and after calcination, showing a sharp decline in the average lifetimes of the calcined samples.

The PL decay traces of all the samples were fitted with a tri-exponential function to calculate the exciton lifetime. Multi-exponential emission decay pattern is observed mainly due to influence of distribution in the recombination rate constants on the decay kinetics. The values of fitting parameter (χ^2), exciton lifetimes (τ_1, τ_2, τ_3), pre-exponential factors (α_1, α_2, α_3) and average exciton lifetimes $<\tau>$ are listed in the table 1

Table 1 The values of fitting parameter (χ^2), exciton lifetimes (τ_1, τ_2, τ_3), pre-exponential factors (α_1, α_2, α_3) and calculated values of average exciton lifetimes $<\tau>$.

Sample (ZnO Cage)	χ^2	τ_1 (ns)	τ_2 (ns)	τ_3 (ns)	α_1	α_1	α_1	$<\tau>$ (ns)
Before calcination	0.99	2.9	21.6	190.7	9.9	18.3	71.8	185.6
After calcination	1.05	2.8	12.5	61.9	44.7	33.9	21.4	46.8

The average lifetime values were calculated using equation (1).[47]

$$<\tau>=\frac{\alpha_1\tau_1^{\,2}+\alpha_2\tau_2^{\,2}+\alpha_3\tau_3^{\,2}}{\alpha_1\tau_1+\alpha_2\tau_2+\alpha_3\tau_3} \qquad (1)$$

From table 1, we have seen that the value of average lifetime, $<\tau>$ is decreased about four times for the calcined ZnO cages as compared to the non-calcined sample. The faster exciton life time of calcined ZnO cages signifies improved charge separation and transport through the tiny 1D ZnO NR building blocks. This may be due to minimized oxygen vacancies in the ZnO cage based photoanode after calcination, also evident from the steady state PL analysis. It is well known that, the oxygen defect sites in the ZnO crystal structure can act as radiative recombination centres for photoexcited electrons and increases the exciton lifetime.[48]

BET surface area analysis

The N_2 adsorption and desorption isotherms of surface area analysis for all the as-synthesized ZnO with different morphologies are shown in the figure 10 (A).

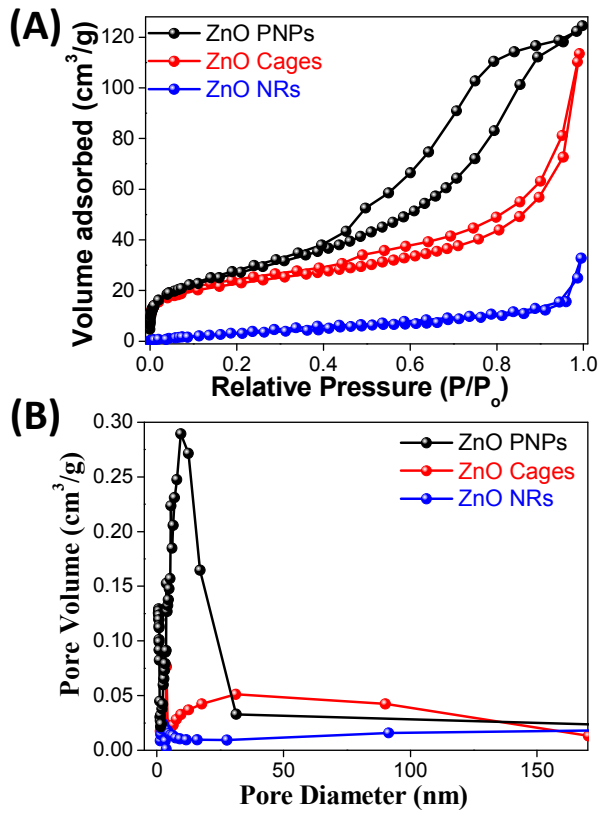

Fig. 10 (A) Nitrogen adsorption–desorption isotherms and **(B)** Barrett–Joyner–Halenda (BJH) pore size distribution plots for as synthesized ZnO PNPs, ZnO cages and ZnO NRs.

It is expected that if a wide band gap semiconductor material (i.e. Photoanodic materials) to be used in dye sensitized solar cell devices (DSSCs), it should have (i) high surface area and (ii) high porosity; in order to achieve a better photovoltaic performance. Type IV isotherms and H3 hysteresis loops observed for ZnO PNPs and ZnO cages, confirm the characteristic mesoporous nature of both the materials. The observed BET surface area of the as-synthesized ZnO PNPs is found to be ~78 m^2g^{-1}, for ZnO cages is ~61 m^2g^{-1}, and for ZnO NR is ~10 m^2g^{-1}. Figure 10(B) demonstrates corresponding Barrett–Joyner–Halenda (BJH) pore size distribution curves for the ZnO heterostructures namely ZnO PNPs (black line), ZnO Cages (red line) and ZnO NRs (blue line). We have observed that pore size distribution for ZnO PNPs is ~10–25 nm and for ZnO cages is in a broad range ~10–150 nm, while there is no indication of pores in case of ZnO NR. The broad range pore size distribution observed in case of ZnO cages is due to presence of two type of pores in them, i.e., (i) pores in between the tiny NRs and (ii) the macro-pores formed due fracture of the multi cages at the adjoining points as we have discussed in the FESEM analysis section.

UV–Visible Absorption spectra and diffused reflectance analysis of the photoanodes

Figure 11(A) demonstrates the normalized UV–vis diffuse reflectance absorption profiles of N719 dye sensitized photoanodes fabricated with as synthesized ZnO heterostructures, i. e. ZnO PNPs, ZnO cages and ZnO NRs. Increasing order of absorbance of the photoanodes in the visible region (~420–700 nm) is observed to be: ZnO NRs< ZnO cages< ZnO PNPs which suggests a higher dye adsorption in the ZnO PNPs and ZnO cages as compared to the ZnO NRs scaffolds. It is well known that, the N719 dye absorb photon energy in the region (420–670 nm) starting the absorption onset from 710 nm. This observation validates the assumption of increase in dye loading capability of a material with increase in surface area. Accordingly, it is expected that the flux of photogenerated electron injection will be higher for ZnO PNP based photoanode relative to the other two photoanodes.

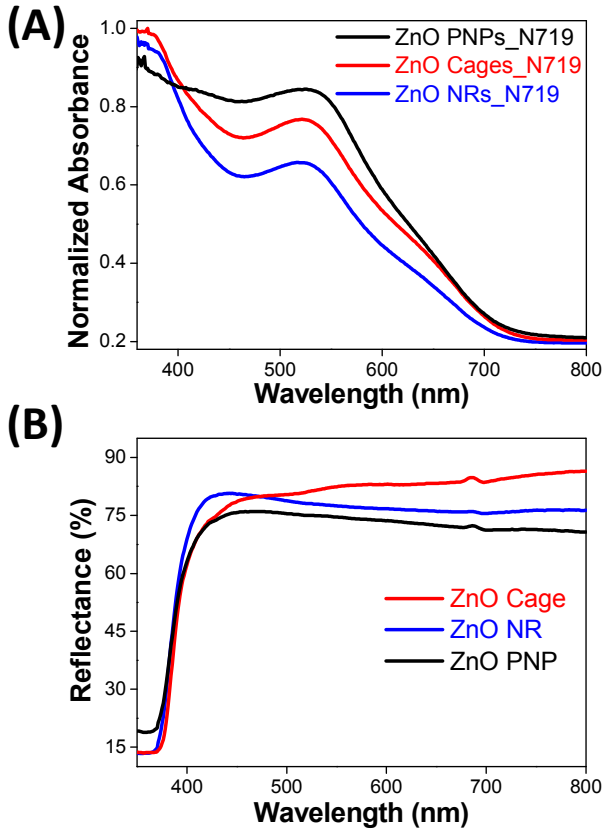

Fig. 11(A) UV-Vis diffused reflectance absorption spectra of all fabricated photoanodes sensitized with N719 dye. **(B)** Diffused reflectance spectra of ZnO cage, ZnO NR and ZnO PNP based films of comparable thickness deposited on the FTO substrates.

Reflectance measurements are carried out for all the photoanode films of comparable thickness based on ZnO cage (red line), ZnO NR (blue line) and ZnO PNP (black line) deposited on FTO substrates to investigate the light scattering effects as depicted in Figure 11 (B). The film based on ZnO cages is exhibiting a distinct higher reflectance in the wavelength range 500–800 nm than that of other two films based on ZnO NRs and ZnO PNPs. This confirms efficient light scattering by the ZnO cages in the photoanode to enhance the repeated excitation process of dye molecules over the ZnO NR and ZnO PNP based photoanodes. Hollow characteristic of ZnO

cages is believed to be the most probable reason for superior light scattering which is not in case of ZnO PNP and ZnO NR based photoanodes. The ZnO NR and ZnO PNP based films have shown similar reflectance ability.

Photovoltaic characteristics of the solar cells

In order to ensure the technological importance and superiority of ZnO cages over the ZnO PNPs, and ZnO NRs; DSSC devices are fabricated and compared their performance parameters. Figure 12(A) represents characteristic current density–voltage (*J–V*) curves for the N719 sensitized ZnO cage, ZnO PNP and ZnO NR based devices. Figure 12 (B) shows IPCE plots for the respective devices.

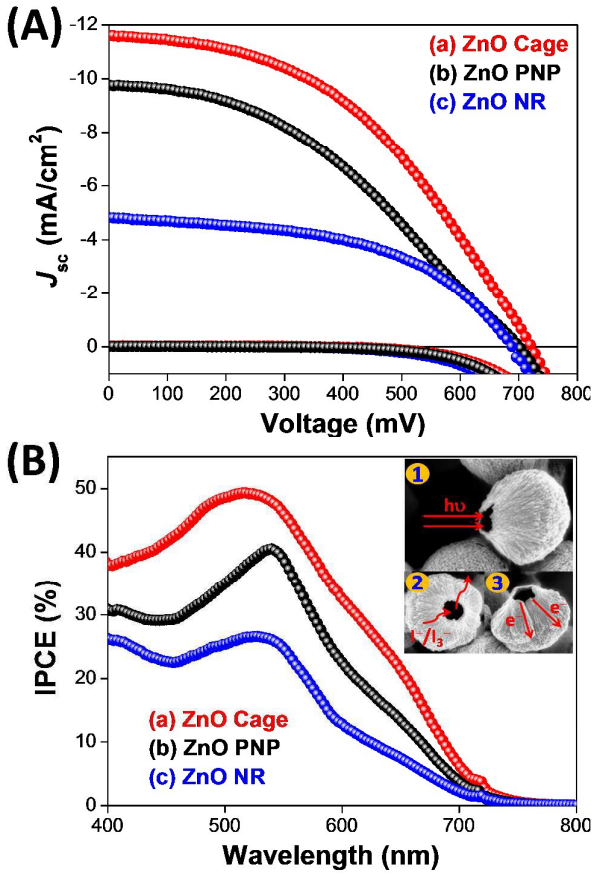

Fig. 12 (A) Current density–Voltage (*J–V*) curves for the photovoltaic devices (a) ZnO Cage [red line], (b) ZnO PNP [black line] and (c) ZnO NR [blue line] **(B)** IPCE plots for the respective devices employing I^-/I_3^- as the redox couple. Inset shows advantages of ZnO cages in terms of light scattering and electron transport in solar cell devices.

The photovoltaic performance parameters such as short circuit current density (J_{sc}), open circuit voltage (V_{oc}), fill factor (FF) and the overall power conversion efficiency (PCE, η) for all the fabricated devices namely, (a) ZnO cage, (b) ZnO PNP, and (c) ZnO NR are listed in table 2.

Table 2. Short-circuit current density (J_{sc}), open-circuit voltage (V_{oc}), fill factor (FF), and power conversion efficiency (η) for the fabricated solar cells incorporating different photoanodes.

Devices	J_{sc} (mAcm^{-2})	V_{oc} (mV)	FF (%)	PCE (%)
(a) ZnO Cage	11.8 (± 0.7)	720 (± 7)	50 (±3)	4.26
(b) ZnO PNP	9.8 (± 0.8)	702 (± 8)	40 (±4)	2.75
(c) ZnO NR	4.8 (±0.7)	690 (±6)	50 (±5)	1.67

Form figure 12 (A) and (B), higher values of J_{sc} and IPCE of ZnO Cage based device (a) [11.8 mA/cm^2 and 50 %] in contrast to the ZnO PNP based device (b) [9.8 mA/cm^2 and 40 %] and ZnO NR based device (c) [4.8 mA/cm^2 and 27 %] are indicating a better absorption of solar irradiation by the device (a), probably due to a better light scattering ability and higher flux of photoinduced electron injection. As explicit from the IPCE plot, better light harvesting ability and red shift towards longer wavelength of about 50 nm of the device (a), is attributed to an efficient light confinement and repeated excitation of dye molecules in the ZnO cage based photoanode.[49, 50] Efficient light confinement in the ZnO Cage based photoanode is expected due to hollow characteristic of ZnO cages and is shown in the inset (1), figure 12(B), which upsurges the value of J_{sc}.[51] Additionally, mesoporous characteristic of ZnO cages expedite the diffusion of electrolyte for better functioning of the redox mediator and the tiny 1-D ZnO NR building blocks act as the transport channels for faster migration of photo-induced electrons to boost the photovoltaic performances [depicted in the insets (2) and (3) to figure 12(B)].[52, 53] Lower values of J_{sc} (~9.8 mA/cm^2) and FF (40 %) for device (b) compared to device (a), even though it have higher dye loading, authenticates the presence of maximum population of crystal defect induced trap sites in ZnO PNPs as discussed in the PL analysis. Similarly, minimum dye loading in ZnO-NR based photoanode is reflected in its low value of J_{sc} (4.8 mA/cm^2) and V_{oc} (690 mV). However, an appreciated value of FF (~50 %) furnished by the device (c) is indicative of facilitated diffusion of electrolyte in the photoanode as compared to the ZnO PNP based photoanode. It is believed that, ZnO NRs in the photoanodic film are randomly arranged and fused to form bigger and higher number of inter-particle pores as compared to the ZnO PNP based photoanodes which expedite the electrolyte diffusion process for better functioning of redox shuttle. Note that, ZnO PNPs have an agglomerated structure of numerous interconnected ZnO NPs which decreases the probability of inter-particle pore formation and smooth diffusion of electrolyte in the photoanodic film. In summary, the enhanced photovoltaic performance parameters of the ZnO cage based device are leading to an appreciated value of PCE (~4.26 %) in current scenario (Table S5, see ESI) which establishes the material to be of good technological importance.

We have investigated morphological features of ZnO cages in the fabricated photoanodes by performing top view and cross-sectional FESEM analysis and shown in the figure 13 for the

stability of the superstructures under rigorous device making conditions.

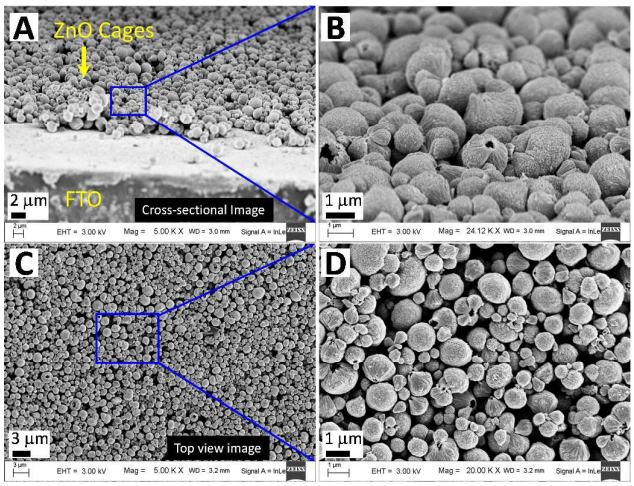

Fig. 13 Cross-sectional (A & B) and top view (C & D) FESEM images of as fabricated ZnO cage based Photoanode.

Figure 13 (A) and (B) are representing cross-sectional FESEM images of ZnO cage based photoanode whereas the (C) and (D) are the top view images. From the FESEM images, it is clear that, cage-like ZnO superstructures remain intact even after the film deposition and calcination processes. This result confirms the beneficial role of hollow and mesoporous characteristics of ZnO cages in its enhanced photovoltaic properties.

Electron transport and recombination kinetics in the photovoltaic devices namely, device (a) ZnO Cage, device (b) ZnO PNP, and device (c) ZnO NR are monitored by employing electrochemical impedance spectroscopy (EIS). Nyquist and Bode phase plots under dark conditions in the frequency range from 0.1 Hz to 100 kHz at an applied bias equivalent to the open-circuit voltages as shown in figure 14 (A) and (B). From the Nyquist plots, i.e. figure 14 (A), the bigger semicircles in the medium-frequency region (right semicircle) specifies the process of charge-transfer at the working electrode/electrolyte interface while the smaller semicircles in the high frequency region (left semicircle) describes the counter electrode/electrolyte interfacial redox reactions.[54] The corresponding Bode phase plots are portrayed in the figure 14 (B). The characteristic peak frequencies in the medium frequency region (f_{max}) for the ZnO Cage, ZnO PNP and ZnO NR based device is located at ~56.2 Hz, ~38.3 Hz and ~36.95 Hz respectively. We have calculated the photo-induced electron life time (τ_e) in the conduction band (CB) of ZnO cage, ZnO PNP and ZnO NR by using the formula (2):[55]

$$\tau_e = \frac{1}{2\pi f_{max}} \qquad (2)$$

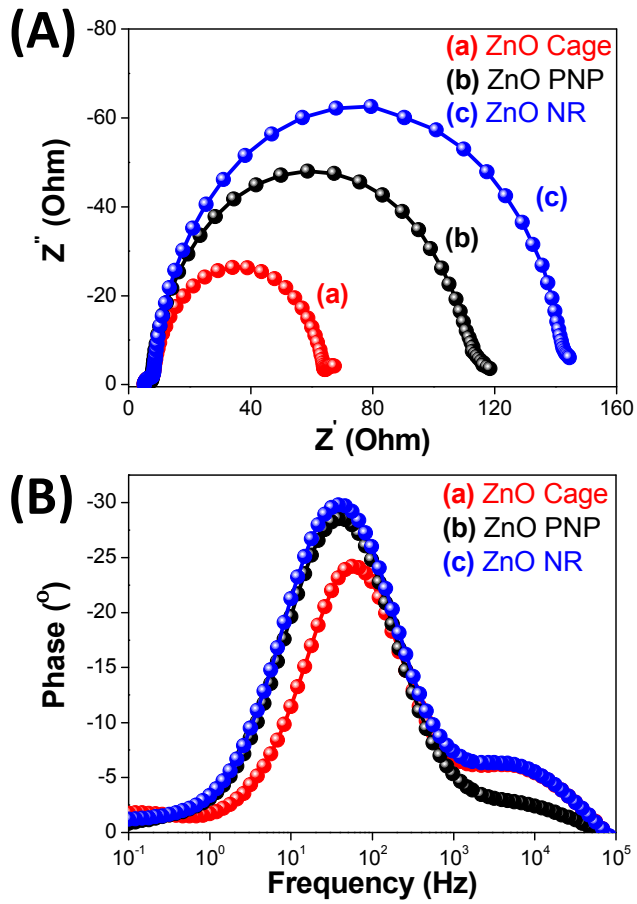

Fig. 14 (A) Nyquist plots for the photovoltaic devices (a) ZnO Cage [red line], (b) ZnO PNP [black line] and (c) ZnO NR [blue line] in dark at open-circuit voltage and in a frequency range from 0.1 Hz to 100 kHz. **(B)** Bode phase plots for all the respective devices.

The τ_e values are found to be ~2.8 ms, ~4.15 ms, and ~4.3 ms for ZnO cage, ZnO PNP and ZnO NR respectively. It is observed from figure 14 (A) that the diameter (R_k) of the right semicircle for the ZnO NR based device is larger in contrast to all other devices. The increasing trend of R_k and life time (τ_e) of the photoinduced electrons in the CB of ZnO heterostructures is ZnO Cage< ZnO PNP< ZnO NR. It is well known that, R_k encompasses the charge recombination resistance and partial contribution from transport resistance.[56] Higher values of R_k and τ_e for ZnO NR based device confirms minimum photoinduced electron interception to the I^-/I_3^- redox shuttle at the ZnO NR/dye/electrolyte interface compared to the ZnO PNPs and ZnO cages respectively which is also reflected in the elevated value of FF (~50 %) for the device.[57, 58] This may be due to single crystalline nature of ZnO NRs and minimum intrinsic defect sites as revealed from TEM and PL analysis respectively which eventually increases the diffusion length of photo-injected electrons. However, flux of photo-induced electrons is expected to be minimum in case of ZnO NR based photoanode due to a lesser amount of adsorption of dye molecules. It is observed that, despite the lower τ_e (~2.8 ms) and R_k values of ZnO Cage based device, the performance of

the device is superior as compared to its counterparts. Injection of high flux of photo-induced electrons in ZnO cage as compared to the device with ZnO NRs overwhelms the efficiency parameters of the device. Additionally, it is established from steady state PL analysis of the photoanodes that the excited state electronic interactions amongst N719 dye molecules and ZnO Cages are stronger as compared to ZnO NRs and ZnO PNPs (Figure S13, see ESI). This confirms faster and an efficient injection of photoinduced electrons from dye molecules to the ZnO cages relative to its counterparts. Moreover, a faster migration of photoinduced electrons through the 1-D ZnO NR building blocks enriches efficient charge transfer to the external circuit. Similar explanation is validated for the ZnO PNP based device (b), in which adsorption of dye is observed to be the highest and probed to be lesser electron interception compared to device (a) with ZnO cages. However, due to a retarded diffusion of electrolyte and higher population of trap sites, the performance of the device is low as compared to the device (a). Lower diffusion of electrolyte in case of ZnO PNP based device is expected due to the agglomerated structure of ZnO PNPs. The agglomerated structure of ZnO PNPs decreases the probability of inter-particle pore formation in the photoanode, which is also reflected in the lower value of FF (~40 %) for the device (b).

Conclusions

We have developed a simple, green hydrothermal synthetic protocol for high quality ZnO superstructures of extensive technological importance utilizing a naturally abundant bio-template "alginic acid". The reaction is investigated in detail by varying synthetic conditions in order to understand the interactions between the organic template and inorganic material. It is found that the optimum concentration of negatively charged alginate ions and NH_4OH in the reaction system are the key factors for formation of these exotic cage like, mesoporous superstructures. A plausible growth mechanism is proposed for the 1-D ZnO NR assembled ZnO superstructures and evaluated their photovoltaic properties. A comparative study on photovoltaic performance parameters of the fabricated dye sensitized solar cells, i.e. based on ZnO cage, ZnO PNP and ZnO NR are carried out. An appreciated value of power conversion efficiency (PCE, η) is furnished by the ZnO cage based devices (η≈ 4.26 %) which is ~60 % and ~35 % improvement over the ZnO NR (η≈ 1.67 %) and ZnO PNP (η≈ 2.75 %) based devices. Enhanced photovoltaic performance of ZnO cage based devices are concluded mainly due to higher flux of photoinduced electrons, enhanced light scattering, probability of facile diffusion of electrolyte and efficient charge separation through nano sized 1-D ZnO NR conduits.

Acknowledgements

We acknowledge Council of Scientific and Industrial Research, India and Department of Science and Technology, India for the financial support through project no. CSIR/01(2704)/12/EMR-II and DST/ TSP/2009/23 respectively. The Infrastructure and instrumentation help from IIT Guwahati and CIF, IIT Guwahati, Institute of Advanced Study in Science and Technology (IASST), Guwahati are hereby acknowledged.

References

1 Y. Liu, J. Goebl and Y. Yin, *Chem. Soc. Rev.*, 2013, **42**, 2610.
2 H. C. Zeng, *J. Mater. Chem.*, 2011, **21**, 7511.
3 W. Shi, S. Song and H. Zhang, *Chem. Soc. Rev.*, 2013, **42**, 5714.
4 T.-D. Nguyen, *Nanoscale*, 2013, **5**, 9455.
5 C. N. R. Rao, H. S. S. Ramakrishna Matte, R. Voggu and A. Govindaraj, *Dalton Trans.*, 2012, **41**, 5089.
6 Z. Chen, Z. Jiao, D. Pan, Z. Li, M. Wu, C.-H. Shek, C. M. L. Wu, and J. K. L. Lai, *Chem. Rev.* 2012, **112**, 3833.
7 H. Zhou, T. Fan and D. Zhang, *ChemSusChem*, 2011, **4**, 1344.
8 H.-B. Yao, H.-Y. Fang, X.-H. Wang and S.-H. Yu, *Chem. Soc. Rev.*, 2011, **40**, 3764.
9 S. Sotiropoulou, Y. Sierra-Sastre, S. S. Mark and C. A. Batt, *Chem. Mater.*, 2008, **20**, 821.
10 R. N. McMillan, C. D. Paavola, J. Howard, S. L. Chan, N. J. Zaluzec and J. D. Trent, *Nat. Mater.*, 2002, **1**, 247.
11 J. Huang, X. Wang and Z. L. Wang, *Nano Lett.*, 2006, **6**, 2325.
12 D. Yang, L. Qi and J. Ma, *Adv. Mater.,* 2002, **14**, 1543.
13 J. He, T. Kunitake and A. Nakao, *Chem. Mater.*, 2003, **15**, 4401.
14 J. Yin, Q. Lu, Z. Yu, J. Wang, H. Pang and F. Gao, *Cryst. Growth Des.*, 2010, **10**, 40.
15 S. R. Hall, H. Bolger and S. Mann, *Chem. Commun.*, 2003, **22**, 2784.
16 Y.-H. Tseng, H.-Y. Lin, M.-H. Liu, Y.-F. Chen and C.-Y. Mou, *J. Phys. Chem. C*, 2009, **113**, 18053.
17 F. Waltz, G. Wißmann, J. Lippke, A. M. Schneider, H.-C. Schwarz, A. Feldhoff, S. Eiden and P. Behrens, *Cryst. Growth Des.*, 2012, **12**, 3066.
18 A.-J. Wang, Q.-C. Liao, J.-J. Feng, P.-P. Zhang, A.-Q. Li and J.-J. Wang, *CrystEngComm*, 2012, **14**, 256.
19 A.-W. Xu, Y. Ma and H. Cölfen, *J. Mater. Chem.*, 2007, **17**, 415.
20 G. Begum, S. V. Manorama, S. Singh and R. K. Rana, *Chem. – Eur. J.*, 2008, **14**, 6421.
21 J. A. Anta, E. Guillen and R. Tena-Zaera, *J. Phys. Chem. C*, 2012, **116**, 11413.
22 N. Linares, A. M. Silvestre-Albero, E. Serrano, J. Sil-vestre-Albero and J. García-Martínez, *Chem. Soc. Rev.*, 2014, **43**, 7681.
23 Q. Zhang, E. Uchaker, S. L. Candelaria and G. Cao, *Chem. Soc. Rev.*, 2013, **42**, 3127.
24 J. Wang, Z. Chen, Y. Liu, C.-H. Shek, C.M. L. Wu and J. K. L. Lai, *Sol. Energy Mater. Sol. Cells*, 2014, **128**, 254.
25 F. Xu and L. Sun, *Energy Environ. Sci.*, 2011, **4**, 818.
26 E. Guillen, L. M. Peter and J. A. Anta, *J. Phys. Chem. C*, 2011, **115**, 22622.
27 N. S. Ramgir, I. S. Mulla and V. K. Pillai, *J. Phys. Chem. B*, 2006, **110**, 3995.
28 H. C. Zeng, *J. Mater. Chem.*, 2006, **16**, 649.
29 F. Chen, F. Cao, H. Li, and Z. Bian, *Langmuir*, 2015, **31**, 3494.
30 Y. Liu, Z. Chen, C.-H. Shek, C. M. L. Wu, and J. K. L. Lai, *ACS Appl. Mater. Interfaces*, 2014, **6**, 9776.
31 R. Huang, Y. Liu, Z. Chen, D. Pan, Z. Li, M. Wu, C.-H. Shek, C. M. L. Wu, and J. K. L. Lai, *ACS Appl. Mater. Interfaces*, 2015, **7**, 3949.

32 G. Li, J. Lan and G. Li, *RSC Adv.*, 2015, **5**, 1705.
33 B. Liu and H. C. Zeng, *J. Am. Chem. Soc.*, 2004, **126**, 16744.
34 J.-J. Feng, Q.-C. Liao, A.-J. Wang and J.-R. Chen, *CrystEngComm*, 2011, **13**, 4202.
35 P. Hu, N. Han, X. Zhang, M. Yao, Y. Cao, A. Zuo, G. Yang and F. Yuan, *J. Mater. Chem.*, 2011, **21**, 14277.
36 B. Liu and H. C. Zeng, *Chem. Mater.*, 2007, **19**, 5824.
37 M. Mo, J. C. Yu, L. Zhang and S.-K. A. Li, *Adv. Mater.*, 2005, **17**, 756.
38 T. R. Chetia, M. S. Ansari and M. Qureshi, *ACS Appl. Mater. Interfaces*, 2015, **7**, 13266.
39 M. Huang, Y. Yan, W. Feng, S. Weng, Z. Zheng, X. Fu and P. Liu, *Cryst. Growth Des.*, 2014, **14**, 2179.
40 A. Mclaren, T. Valdes-Solis, G. Li and S. C. Tsang, *J. Am. Chem. Soc.*, 2009, **131**, 12540.
41 Q. Yu, W. Fu, C. Yu, H. Yang, R. Wei, M. Li, S. Liu, Y. Sui, Z. Liu, M. Yuan and G. Zou, *J. Phys. Chem. C*, 2007, **111**, 17521.
42 Z. Wang, X. F. Qian, J. Yin and Z. K. Zhu, *J. Sol-id State Chem.*, 2004, **177**, 2144.
43 X. M. Sun, X. Chen, Z. X. Deng and Y. D. Li, *Mater. Chem. Phys.*, 2002, **78**, 99.
44 K. Govender, D. S. Boyle, P. B. Kenway and P. O'Brien, *J. Mater. Chem.*, 2004, **14**, 2575.
45 H. Zeng, G. Duan, Y. Li, S. Yang, X. Xu and W. Cai, *Adv. Funct. Mater.*, 2010, **20**, 561.
46 X. L. Wu, G. G. Siu, C. L. Fu and H. C. Ong, *Appl. Phys. Lett.*, 2001, **78**, 2285.
47 A. Kongkanand, K. Tvrdy, K. Takechi, M. Kuno, P. V. Kamat, *J. Am. Chem. Soc.,* 2008, **130**, 4007.
48 H.-M. Cheng, K.-Y. Huang, K.-M. Lee, P. Yu, S.-C. Lin, J.-H. Huang, C.-G. Wu, J. Tang, *Phys. Chem. Chem. Phys.*, 2012, **14**, 13539.
49 D. Barpuzary and M. Qureshi, *ACS Appl. Mater. Interfaces*, 2013, **5**, 11673.
50 T. R. Chetia, D. Barpuzary and M. Qureshi, *Phys. Chem. Chem. Phys.*, 2014, **16**, 9625.
51 M. Qureshi, T. R. Chetia, M. S. Ansari and S. S. Soni, *J. Mater. Chem. A*, 2015, **3**, 4291.
52 R. Plass, S. Pelet, J. Krueger, M. Grätzel and U. Bach, *J. Phys. Chem. B*, 2002, **106**, 7578.
53 D. Barpuzary, A. Banik, A. N. Panda and M. Qureshi, *J. Phys. Chem. C*, 2015, **119**, 3892.
54 S. Phadke, A. D. Pasquier and D. P. Birnie, *J. Phys. Chem. C*, 2011, **115**, 18342.
55 R. Kern, R. Sastrawan, J. Ferber, R. Stangl and J. Lu-ther, *J. Electrochim. Acta*, 2002, **47**, 4213.
56 J. Tian, E. Uchaker, Q. Zhang and G. Cao, *ACS Appl. Mater. Interfaces*, 2014, **6**, 4466.
57 D. Barpuzary; A. S. Patra, J. V. Vaghasiya, B. G. Solanki, S. S. Soni and M. Qureshi, *ACS Appl. Mater. Interfaces*, 2014, **6**, 12629.
58 W. Peng, L. Han and Z. Wang, *Chem.– Eur. J.*, 2014, **20**, 8483.